

DashGaussian: Optimizing 3D Gaussian Splatting in 200 Seconds

Youyu Chen^{1#} Junjun Jiang^{1†} Kui Jiang¹ Xiao Tang²
 Zhihao Li² Xianming Liu¹ Yinyu Nie²
¹Harbin Institute of Technology ²Huawei Noah’s Ark Lab

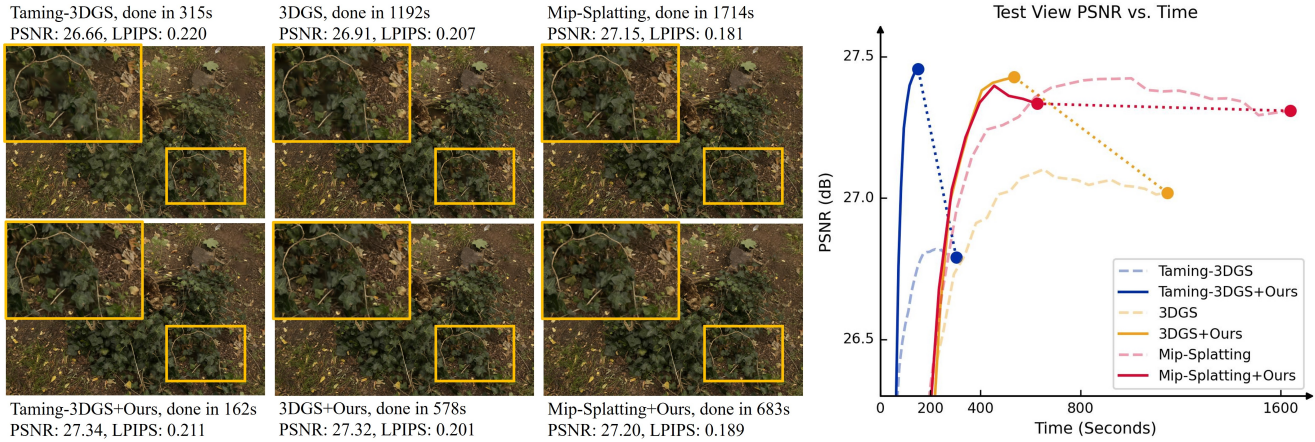


Figure 1. We propose DashGaussian, a fast 3D Gaussian Splatting (3DGS) optimization method that can be easily plugged into existing 3DGS backbones. DashGaussian significantly boosts the training speed of various 3DGS backbones by **45.7%** on average without trading off rendering quality. Equipping DashGaussian to prior-art 3DGS methods, we reduce the optimization time of a 3DGS model with millions of primitives to **200 seconds** on a consumer-grade GPU. The figures above show the scene “stump” in the Mip-NeRF 360 dataset.

Abstract

3D Gaussian Splatting (3DGS) renders pixels by rasterizing Gaussian primitives, where the rendering resolution and the primitive number, concluded as the optimization complexity, dominate the time cost in primitive optimization. In this paper, we propose DashGaussian, a scheduling scheme over the optimization complexity of 3DGS that strips redundant complexity to accelerate 3DGS optimization. Specifically, we formulate 3DGS optimization as progressively fitting 3DGS to higher levels of frequency components in the training views, and propose a dynamic rendering resolution scheme that largely reduces the optimization complexity based on this formulation. Besides, we argue that a specific rendering resolution should cooperate with a proper primitive number for a better balance between computing redundancy and fitting quality, where we schedule the growth of the primitives to synchronize with the rendering resolution. Extensive experiments show that our method accelerates the optimization of various 3DGS backbones by 45.7% on average while preserving the rendering quality. Project page is available at dashgaussian.github.io.

1. Introduction

Novel view synthesis has long been investigated as an important branch of 3D scene reconstruction. Neural Radiance Field (NeRF) [33] as a milestone work has largely improved the visual quality of novel views, but at the cost of days to optimize a single scene. Though many efforts [6–8, 11, 17, 30, 34, 44] have been made to improve the efficiency, NeRF-based methods still face challenges in balancing the optimization time and rendering quality. In contrast, 3D Gaussian Splatting (3DGS) [22] utilizes Gaussian primitives to model a scene, achieving equivalent novel view rendering quality as NeRF while reducing the optimization time of one scene to tens of minutes. Nevertheless, there remains a high demand for further acceleration to enable 3DGS applications on devices with limited computational power or in large-scale, time-intensive scene reconstruction tasks [27, 29, 31, 49].

Given a specific 3DGS backbone, there are multiple strategies to accelerate its optimization, which can be collected into two major categories. From an engineering per-

[#]This work was done during he was an intern at Huawei.

[†]Corresponding author. E-mail: jiangjunjun@hit.edu.cn.

spective, some works [10, 12, 15, 32, 45] accelerate the optimization by refining the rendering pipeline to enable high-efficiency computation. From an algorithmic perspective, some works [13, 35] propose to prune redundant Gaussian primitives after primitive densification. While these algorithmic methods perform effectively, the rendering quality noticeably declines when a considerable number of parameters are excluded to speed up the optimization.

Instead of eliminating redundant Gaussian primitives, we pursue an effective strategy for allocating computational resources, which smartly leverages each Gaussian primitive to be more time-efficiently optimized. This is based on three key observations. First, in 3DGS optimization, computational resources are primarily consumed by three main operations — forward rendering, gradient back-propagation, and primitive update — all of which have their computational complexity commonly relying on the rendering resolution and the number of Gaussian primitives. Second, rendering high-resolution images at the beginning of optimization is thrifless because the primitives are sparse at this stage. Third, the late stage of the optimization consumes a huge portion of time cost because of the large primitive number while bringing limited rendering quality improvement (see the curves of backbones in Fig. 1). These observations inspire us to propose a more effective allocation of computational resources for current 3DGS methods. For simplicity, we refer to the rendering resolution and the number of primitives collectively as the ‘optimization complexity’. By manipulating the optimization complexity on different optimization stages, one can arbitrarily customize the computational resource distribution. Naively reducing optimization complexity can promisingly achieve acceleration though, it usually trades off the rendering quality.

One way to manipulate the optimization complexity is to reduce the rendering resolution in the early stage of 3DGS optimization. However, simply reducing the resolution in training results in 3D aliasing [28, 47], which sacrifices the rendering fidelity in the original resolution. Nevertheless, according to image processing theory, when comparing two images — one downsampled from the other — the key difference between them lies in the residual frequency components involved in the high-resolution image but absent in the low-resolution one [18]. This indicates that increasing the rendering resolution during the optimization process is equivalent to gradually fitting 3DGS to higher levels of frequency components in the training views (see Fig. 2). Inspired by this, we propose a scene-adaptive frequency-based resolution scheduling scheme that progressively increases the rendering resolution throughout the entire optimization process while ensuring its fidelity at the end.

Given the scheduled rendering resolution, we point out that a specific rendering resolution should be paired with an appropriate number of Gaussian primitives to better bal-

ance the computational redundancy and fitting quality of 3DGS. To this end, we design a primitive number scheduler that tames the primitives to grow simultaneously with the rendering resolution by coupling them with a numerical constraint. This scheduler produces a concave-up curve depicting the growth of the primitive, which spans over the entire optimization process (see Fig. 2). Such a concave-up growth curve possesses significant advantage over the ones in existing works that are either concave-down [22, 32] or reach their peak at half of the optimization iterations [5, 22]. Moreover, we introduce a momentum-based primitive budgeting method to adaptively estimate the maximum number of primitives in the growth curve, rather than relying on dataset priors as in existing methods [5, 13, 23, 32].

We integrate the proposed resolution scheduler and the primitive scheduler, presenting DashGaussian, which significantly accelerates the optimization process across various 3DGS backbones by 45.7% on average without trading off the rendering quality. To summarize our contributions,

- We speed up the optimization of 3DGS by reasonably distributing the computational resources throughout the optimization process.
- We propose a scheduling method to corporately control the growth of rendering resolution and Gaussian primitives, ensuring that the rendering quality is maintained.
- We design an adaptive Gaussian primitive budgeting method to determine the primitive number demanded by the scene, releasing primitive growth scheduling from appointing the final primitive number heuristically.

2. Related Work

Novel View Synthesis. Among the vast amount of investigations on novel view synthesis [4, 9, 16, 36, 38], Neural Radiance Fields (NeRF) [33] have achieved particular success, but at the cost of tens of hours to optimize for a single scene [1, 2, 19, 33, 34, 42]. Although there have been many works focusing on improving NeRF’s efficiency [6, 8, 17, 30, 34, 44, 51], they still struggle with balancing the optimization efficiency and rendering quality. Alternatively, 3D Gaussian Splatting (3DGS) [22] emerges as a solution that possesses comparable rendering quality to NeRF together with significant advancement in terms of the speed of both optimization and rendering. The efficiency of 3DGS benefits from its GPU-friendly rendering pipeline, which largely reduces the computational burden for its optimization. 3DGS has been widely applied in different tasks, such as large scene reconstruction [29, 31, 49], digital human [26, 46], and 3D segmentation [20, 40]. Improving the performance of 3DGS is fundamental and significant to benefit the downstream tasks.

Acceleration for 3DGS Optimization. Since the success of 3DGS is largely driven by its computational efficiency, it

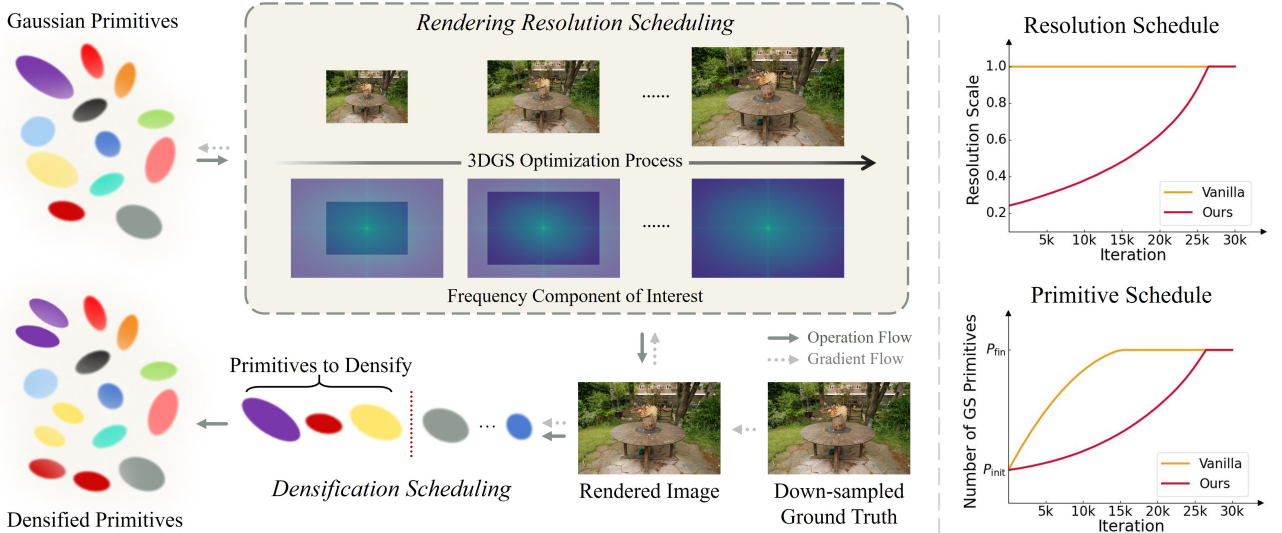


Figure 2. **The pipeline of DashGaussian.** DashGaussian determines the rendering resolution for each 3DGS optimization step with our resolution scheduling method. The insight of the resolution scheduling is to gradually fit 3DGS to higher level of frequency components in the training views throughout the entire optimization process. By directing the downsampling of training views with our scheduler, we significantly reduce the time cost for 3DGS optimization while preserving the rendering quality. We further manage the growth of Gaussian primitives, which cooperates with the scheduled rendering resolution. It prevents possible over-densification issues during the low-resolution optimization phase and further accelerates the optimization with suppressed primitive growth.

is intuitive to further improve its speed with high-efficiency computation. By refining the implementation of forward-pass, backward-pass and parameter update of 3DGS, recent works [12, 14, 32, 45] accelerate the optimization of 3DGS by a large margin. Meanwhile, reducing the parameters of 3DGS is also a promising option to accelerate the optimization. For example, Fang and Wang [13] propose to reduce the number of Gaussian primitives by pruning the crowded primitives. Papantonakis *et al.* [35] further propose to strip the redundant appearance descriptors of each primitive to reduce the optimized parameters. However, these methods inevitably hinder the rendering quality because of their hard cropping operation to shrink the size of the original 3DGS model. In contrast, DashGaussian ingeniously suppresses the optimization complexity and densifies Gaussian primitives without hard cropping, thus holding the potential to preserve the rendering quality.

Scheduled 3DGS Optimization 3DGS [22] densifies the Gaussian primitives, which results in an unpredictable size of the optimized Gaussians. To make the densification controllable, Mallick *et al.* [32] propose to mimic the primitive growth of 3DGS [22] with a constructive densification process. Bulò *et al.* [5] propose to densify the Gaussian primitive by a constant ratio until the predetermined primitive budget is met. On the other hand, 3DGS with Level of Details (LoD) [39, 41] is optimized with multiple rendering resolutions for seamlessly rendering at varying levels of

details. However, these methods are time-consuming in optimization while their levels of resolution are fixed. DashGaussian corporately schedules both rendering resolution and primitive growth in an adaptive manner, which significantly boosts the optimization of 3DGS without predetermining the final primitive number heuristically.

3. Preliminary

Given a set of posed images capturing a scene and the corresponding point cloud derived from the structure-from-motion algorithm [37], 3DGS optimizes a set of 3D Gaussian primitives $\{\mathcal{G}_i(\mathbf{x}) = e^{-\frac{1}{2}(\mathbf{x}-\mathbf{p}_i)\Sigma_i^{-1}(\mathbf{x}-\mathbf{p}_i)}\}_{i=1}^P$ to represent the scene for novel view synthesis. Each 3D Gaussian primitive \mathcal{G}_i is characterized with its center position $\mathbf{p}_i \in \mathbb{R}^3$, covariance matrix defined in the world space $\Sigma_i \in \mathbb{R}^{3 \times 3}$, opacity $o_i \in (0, 1)$ and color coefficients \mathbf{c}_i . Here, P is the total number of Gaussian primitives used to represent the scene. To render images of camera views, 3DGS splats these Gaussian primitives onto pixels. The color \mathbf{C} of a pixel \mathbf{u} is calculated as

$$\mathbf{C}(\mathbf{u}) = \sum_{i=1}^P T_i(\mathbf{u}) \cdot w_i(\mathbf{u}) \cdot \mathbf{c}_i, \quad T_i(\mathbf{u}) = \prod_{j=1}^{i-1} (1 - w_j(\mathbf{u})), \quad (1)$$

where $w_i(\mathbf{u}) = o_i \mathcal{G}_i^{2D}(\mathbf{u})$, and \mathcal{G}_i^{2D} denotes the 2D Gaussian splatted to the image plane from \mathcal{G}_i . As the whole

process is fully differentiable, \mathcal{G}_i can be optimized by back-propagating the gradients from losses between renderings and training images. The number of rendered pixels, decided by the rendering resolution, indicates the times Eq. (1) is processed, thus directly affecting the optimization time. The original 3DGS algorithm [22] further incorporates a densification operation during the optimization process, which identifies those \mathcal{G}_i in under-reconstructed regions and then clones or splits them to better represent the scene. As the Gaussian primitive number P increases, the computational burden in Eq. (1) also grows, which directly impacts optimization efficiency. We collectively refer to the rendering resolution and the number of primitives as optimization complexity, and our goal is to reduce the overall optimization complexity to accelerate 3DGS optimization.

4. DashGaussian

In this section, we introduce how DashGaussian strips the optimization complexity to accelerate 3DGS optimization without trading off rendering quality. Sec. 4.1 reviews the aliasing issue in image downsampling, and proposes to formulate optimizing 3DGS with increasing rendering resolution as fitting to different level of frequency components. In Sec. 4.2, we introduce our frequency-guided resolution scheduling strategy, which adaptively builds the resolution schedule for each scene based on the frequency component of training views. In Sec. 4.3, we introduce our resolution-guided primitive scheduling scheme, which tames the number of Gaussian primitives to grow simultaneously with the rendering resolution, establishing a reasonable cooperation between the rendering resolution and the primitive number.

4.1. Problem Formulation

Optimizing 3DGS with images in different resolutions while maintaining high rendering fidelity is non-trivial. More concretely, we discuss the case where 3DGS is supervised with downsampled low-resolution (LR) images while aiming to render the original high-resolution (HR) ones. We investigate this problem as it inevitably leads to 3D aliasing [47], making it formidable to accelerate the optimization with LR supervision while keeping a high fidelity in HR rendering. However, viewing 3DGS optimization through the lens of 2D image reconstruction, the frequency theory in image processing offers a fresh perspective.

We first review image downsampling, which is applied to the training views to decrease their resolution. Given an image $\mathbf{I} \in \mathbb{R}^{H \times W}$ being downsampled to $\mathbf{I}_r \in \mathbb{R}^{\frac{H}{r} \times \frac{W}{r}}$, we denote their frequency maps with Discrete Fourier Transform (DFT) by $\mathbf{F} = \text{DFT}(\mathbf{I}) \in \mathbb{R}^{H \times W}$ and $\mathbf{F}_r = \text{DFT}(\mathbf{I}_r) \in \mathbb{R}^{\frac{H}{r} \times \frac{W}{r}}$, respectively. According to the Nyquist Sampling Theorem, one can never recover \mathbf{I} from

\mathbf{I}_r if the sampling frequency of \mathbf{I}_r is less than two times of the maximum frequency contained in \mathbf{F} . Meanwhile, a simple spatial downsampling could result in aliasing issues that disturb the recoverable low-frequency components and introduce artifacts in \mathbf{I}_r . To address this issue, anti-aliasing downsampling methods apply a low-pass filter on \mathbf{F} in different ways before downsampling \mathbf{I} . The most straightforward way is to center crop \mathbf{F} to the size of $(H/r, W/r)$, scale its numerical value by $1/r^2$, then inversely transform the cropped \mathbf{F} into \mathbf{I}_r .

With the above analysis, we see the key difference between \mathbf{I} and \mathbf{I}_r is the residual high-frequency component that \mathbf{F} embeds while \mathbf{F}_r does not. Based on this observation, we reformulate optimizing 3DGS with increasing image resolutions by gradually fitting 3DGS to higher levels of frequency components throughout the entire optimization process (see Fig. 2). In Sec. 4.2, we demonstrate that this formulation indicates the extent to which downsampled images can be used to optimize a 3DGS model.

4.2. Frequency Guided Resolution Scheduler

Based on the discussion in Sec. 4.1, we propose to schedule the rendering resolution of 3DGS throughout the optimization process, which adaptively distributes optimization steps to different resolutions based on the amount of information contained in the frequency domain of each resolution. Since our scheduling covers the entire optimization process, we can largely reduce the optimization complexity and reduce the overall time cost. For simplicity, only two different resolutions (H, W) and $(H/r, W/r)$, whose related notations are defined the same as Sec. 4.1, are introduced in the following discussion to optimize 3DGS, where $r \geq 1$. The LR rendering $(H/r, W/r)$ is applied in the early stage of optimization, which is switched to HR rendering (H, W) by the end. Here we suppose the LR training views for supervision are aliasing freely downsampled from the HR training views.

The key problem is when to increase the rendering resolution from low to high, solving which is equivalent to answering how to distribute the total S optimization steps between \mathbf{F} and \mathbf{F}_r . Since \mathbf{F}_r is contained within \mathbf{F} because \mathbf{I} is aliasing freely downsampled to \mathbf{I}_r , the frequency component in LR images is always accessible in all the S iterations for supervision. The question is to know the ‘significance’ of the HR images and decide the portion they take in the S steps to preserve HR rendering fidelity of 3DGS.

A reasonable definition of the significance should handle both 2D and 3D aliasing issue during optimization. Because 2D aliasing happens in the frequency domain, it indicates a significance definition based on a numerical feature of the frequency map, e.g., the frequency energy which dominates the optimization steps with the LR rendering. On the other hand, 3D aliasing has been thoroughly discussed

by Mip-Splatting [47]. Though Mip-Splatting alleviated the 3D aliasing issue, it still encourages optimization in HR for high-fidelity HR rendering.

To balance these two issues, we define the significance of images under a specific resolution (h, w) as

$$\mathcal{X}(\mathbf{F}) = \frac{1}{N} \sum_{n=1}^N \sum_{i=1}^h \sum_{j=1}^w \|\mathbf{F}^n(i, j)\|_2, \quad (2)$$

where $\mathbf{F}^n = \text{DFT}(\mathbf{I}^n)$; $\{\mathbf{I}^n\}_{n=1}^N$ are the training views sampled with the resolution of (h, w) , and N is the number of training views. Derived from numerical feature in the frequency domain, this definition particular emphasizes the high-frequency component. Intuitively, if $\mathcal{X}(\mathbf{F}) - \mathcal{X}(\mathbf{F}_r)$ is far bigger than $\mathcal{X}(\mathbf{F}_r)$, the optimization steps should be dominated with the HR rendering, and vice versa. Following this intuition, we define a fraction function by

$$f(\mathbf{F}, \mathbf{F}_r) = \frac{\mathcal{X}(\mathbf{F}) - \mathcal{X}(\mathbf{F}_r)}{\mathcal{X}(\mathbf{F})}, \quad (3)$$

with which we distribute $S \cdot f(\mathbf{F}, \mathbf{F}_r)$ iterations to the HR rendering. In other words, we should increase the rendering resolution from $(H/r, W/r)$ to (H, W) at the s_r -th iteration, where $s_r = S \cdot (1 - f(\mathbf{F}, \mathbf{F}_r)) = S \cdot \mathcal{X}(\mathbf{F}_r)/\mathcal{X}(\mathbf{F})$.

In practice, we can generalize the above discussion and adapt Eq. (3) to the case with multiple intermediate resolutions. Given a group of downsampling factors r_1, r_2, \dots, r_m that monotonically increase, indicating downsampled images $\mathbf{I}_{r_m}, \dots, \mathbf{I}_{r_1}, \mathbf{I}$ are progressively involved for supervision throughout the optimization process, we increase the rendering resolution from $(H/r_i, W/r_i)$ to $(H/r_{i-1}, W/r_{i-1})$ at the s_{r_i} -th iteration.

We correspond the maximal downsampling factor r_m with the one whose $\mathcal{X}(\mathbf{F}_{r_m}) = \frac{1}{a} \mathcal{X}(\mathbf{F})$, where a is a hyper-parameter (defaulted by 4). We linearly sample the rest $\mathcal{X}(\mathbf{F}_{r_1}), \dots, \mathcal{X}(\mathbf{F}_{r_{m-1}})$ between $\mathcal{X}(\mathbf{F})$ and $\mathcal{X}(\mathbf{F}_{r_m})$, and solve the corresponding resolution factors r_1, \dots, r_{m-1} . The rendering resolution $r^{(k)}$ for iteration k between s_{r_i} and $s_{r_{i-1}}$ is interpolated with the inverse square of r_i and r_{i-1} . Please refer to the supplementary for more details.

By programming the rendering resolution throughout the optimization process of 3DGS with the scheduling scheme above (see the curve in Fig. 2), we significantly reduce the optimization time while maintaining or even improving the quality of the optimized 3DGS, which is revealed by the experiments in Sec. 5.3.

4.3. Resolution Guided Primitive Scheduler

Recent works have revealed the fact that over-dense Gaussian primitives only marginally improves rendering quality, but largely slows down the optimization [13, 35]. To further improve the efficiency of DashGaussian, it is vital for

the growth of primitives to avoid over densification in the LR optimization stage and determine a proper number of Gaussian primitives in the optimized 3DGS model.

Resolution Guided Densification. Since 3DGS is supervised with images capturing the surface of the scene, which the Gaussian primitives majorly describe [13, 21, 48], thus the number of primitives should correlate to the level of detail describing the surface, which can be approximated as the number of pixels covering the scene. Specifically, denoting the initial primitive number as P_{init} , and the desired primitive number in the final 3DGS model as P_{fin} , we control the primitive number of the i -th iteration by

$$P_i = P_{\text{init}} + (P_{\text{fin}} - P_{\text{init}}) / \left(r^{(i)}\right)^{2-i/S}, \quad (4)$$

where $r^{(i)}$ denotes the rendering resolution of the i -th iteration, powered by a factor of $2 - i/S$. In practice, we find too much growth of primitives by the end of optimization will result in poor convergence of the primitives, which significantly hinders the quality of the optimized 3DGS model. So we gradually decrease the power factor from 2 to 1 along the optimization process to suppress the primitive number in the early optimization while encouraging its growth in the mid-stage of optimization. Such a scheduling scheme produces a concave-up function depicting the relation between the primitive number and optimization steps with a small area under the curve (see Fig. 2), which largely reduces the optimization complexity.

Momentum-based Primitive Budgeting. Recent methods obtain P_{fin} relying on the dataset prior [5, 13, 32], such as simply setting P_{fin} as a multiple of P_{init} [32], which is a rule of thumb and cannot explain if it is enough for fitting a scene. We address this problem alternatively by determining P_{fin} along the optimization process, instead of determining it ahead of optimization.

Specifically, inspired by the momentum optimizer [24], which updates the parameters of a learning model with the accumulated gradients simulating the physical momentum, we regard P_{fin} as the momentum and the number of primitives naturally densified in each step as the force (denoted as P_{add}). Then we calculate P_{fin} as

$$P_{\text{fin}}^{(i)} = \max(P_{\text{fin}}^{(i-1)}, \gamma \cdot P_{\text{fin}}^{(i-1)} + \eta \cdot P_{\text{add}}^{(i)}), \quad (5)$$

where γ, η are hyper-parameters (defaulted by 0.98 and 1 in this paper), i denotes the i -th optimization step. The maximum operator is applied to keep $P_{\text{fin}}^{(i)}$ monotonously increasing along the optimization process. With Eq. (5), we dynamically update P_{fin} in Eq. (4), where $P_{\text{fin}}^{(0)}$ is initialized as $5 \cdot P_{\text{init}}$. Experiments show that this momentum-based scheme performs effectively across various datasets, releasing densification scheduling from the need to specify an upper bound for the primitive growth.

Table 1. Quantitative comparisons with existing 3DGS fast optimization methods. With DashGaussian, we finish 3DGS optimization within 200 seconds while achieving significantly higher rendering quality compared with the other methods. “Ours” in the table reports the performance of equipping DashGaussian to Taming-3DGS¹ [32]. Time is reported in minutes.

Method	MipNeRF-360 [3]					Deep Blending [19]					Tanks and Temples [25]				
	$N_{GS} \downarrow$	PSNR \uparrow	SSIM \uparrow	LPIPS \downarrow	Time \downarrow	$N_{GS} \downarrow$	PSNR \uparrow	SSIM \uparrow	LPIPS \downarrow	Time \downarrow	$N_{GS} \downarrow$	PSNR \uparrow	SSIM \uparrow	LPIPS \downarrow	Time \downarrow
3DGS [22]	3.12M	27.72	0.826	0.201	18.31	2.82M	29.50	0.904	0.244	17.27	1.83M	23.62	0.847	0.177	10.59
Reduced-3DGS [35]	1.44M	27.28	0.813	0.222	15.52	0.98M	29.78	0.907	0.245	13.74	0.65M	23.59	0.844	0.185	8.31
Mini-Splatting [13]	0.49M	27.22	0.821	0.217	14.72	0.34M	29.95	0.907	0.253	12.91	0.20M	23.20	0.835	0.201	8.66
Taming-3DGS [32]	2.28M	27.61	0.821	0.210	5.51	2.32M	29.69	0.906	0.245	4.52	1.51M	23.62	0.849	0.174	4.02
DashGaussian (Ours)	2.04M	27.92	0.826	0.208	3.23	1.94M	30.02	0.907	0.248	2.20	1.19M	23.97	0.851	0.180	2.62

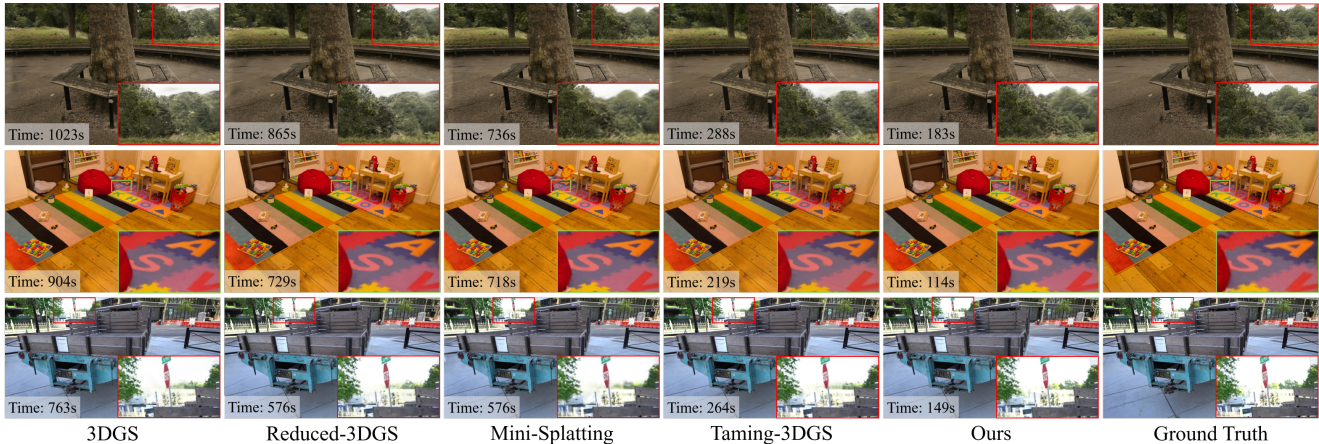


Figure 3. Qualitative results of Tab. 1. We show the rendering results of the “treehill” scene in the Mip-NeRF 360 dataset [3], the “playroom” scene in the Deep Blending dataset [19], and the “truck” scene in the Tanks&Temples dataset [25], respectively.

5. Experiments

Datasets. We conduct experiments on three real-world datasets, Mip-NeRF 360 [3], Deep-Blending [19], and Tanks&Temples [25], respectively. For fair comparisons, we process these datasets following vanilla 3DGS [22]. We also perform evaluation on MatrixCity dataset [27] for large-scale reconstruction in supplementary.

Metrics. To evaluate novel view rendering quality, we report average PSNR (peak signal-to-noise ratio), SSIM [43], and LPIPS [50] on each dataset. We also report the average total optimization time in minutes to measure the optimization speed. Furthermore, we also report the average primitive number of the optimized 3DGS model on each dataset, which gives an overall evaluation on per-primitive contribution to novel view rendering quality.

Implementation Details. The resolution downsampling factor $r^{(i)}$ defined in Sec. 4.2 is a continuous scalar (see Fig. 2). In practice, we modulate $r^{(i)}$ with $r^{(i)} = \lfloor r^{(i)} \rfloor$ (see Fig. 4). Such a modulation encourages the Gaussian primitives to grow relatively faster against the case without modulation, optimizing each Gaussian primitive more sufficiently to keep the novel view rendering quality.

When we plug DashGaussian to backbones, the hyper-parameters of each backbone are kept unchanged as their official implementations. All experiments are conducted on a single GPU with about 80 TFLOPS for FP32. Please refer to the supplementary for more implementation details.

5.1. Comparison with Fast Optimization Methods

Baselines. We report the comparisons with the state-of-the-art fast optimization methods, i.e., Reduced-3DGS [35], Mini-splatting [13] and Taming-3DGS [32] in Tab. 1. Reduced-3DGS and Mini-Splatting achieve acceleration by pruning low contribution parameters, and Taming-3DGS obtains its speed for efficient back-propagation and Sparse Adam optimizer. These three methods are representative for algorithmic and engineering fast optimization methods.

Quantitative Results. By plugging DashGaussian to Taming-3DGS [32], we accomplish the optimization of 3DGS within 200 seconds, which is reported in Tab. 1. Among all the methods in Tab. 1, DashGaussian shows a significant improvement in the optimization speed over ex-

¹Taming-3DGS [32] referred to in this paper only includes efficient backward implementation and Sparse Adam optimizer.

Table 2. Quantitative results of accelerating various 3DGS backbones using DashGaussian. Plugging DashGaussian into different backbones, their optimization speed is largely improved by 45.7% on average. Most prominently, DashGaussian achieves acceleration with negligible compromise and even improvement in the rendering quality. The results advocate that a reasonable computational resource allocation across the optimization process can largely boost the optimization while preserving the rendering quality. ‘‘Revising-3DGS*’’ denotes our reproduction of the paper [5] based on the Taming-3DGS [32] codebase. Time is reported in minutes.

Method	MipNeRF-360 [3]					Deep Blending [19]					Tanks and Temples [25]				
	$N_{GS} \downarrow$	PSNR \uparrow	SSIM \uparrow	LPIPS \downarrow	Time \downarrow	$N_{GS} \downarrow$	PSNR \uparrow	SSIM \uparrow	LPIPS \downarrow	Time \downarrow	$N_{GS} \downarrow$	PSNR \uparrow	SSIM \uparrow	LPIPS \downarrow	Time \downarrow
3DGS [22]	3.12M	27.72	0.826	0.201	18.31	2.82M	29.50	0.904	0.244	17.27	1.83M	23.62	0.847	0.177	10.59
+Ours	2.69M	27.81	0.828	0.203	10.16	2.18M	29.29	0.901	0.256	8.16	1.43M	23.83	0.844	0.189	6.13
Mip-Splatting [47]	3.97M	27.91	0.838	0.174	25.83	3.48M	29.26	0.902	0.239	23.57	2.36M	23.75	0.859	0.156	14.23
+Ours	3.14M	27.99	0.835	0.186	12.60	2.55M	29.55	0.903	0.248	9.80	1.62M	23.96	0.856	0.172	6.13
Revising-3DGS* [5]	1.94M	27.65	0.826	0.194	5.73	2.02M	29.54	0.906	0.248	4.06	1.32M	23.87	0.856	0.168	4.50
+Ours	1.94M	27.85	0.833	0.191	3.46	2.02M	29.76	0.907	0.251	2.21	1.32M	23.85	0.853	0.176	3.16
Taming-3DGS [32]	2.28M	27.61	0.821	0.210	5.51	2.32M	29.69	0.906	0.245	4.52	1.51M	23.62	0.849	0.174	4.02
+Ours	2.04M	27.92	0.826	0.208	3.23	1.94M	30.02	0.907	0.248	2.20	1.19M	23.97	0.851	0.180	2.62

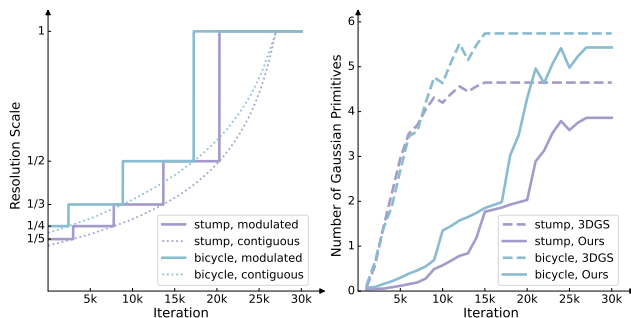


Figure 4. Variation in the optimization complexity. The left shows that DashGaussian scene-adaptively schedules the rendering resolution for the scenes ‘‘bicycle’’ and ‘‘stump’’ from Mip-NeRF 360 dataset. Please refer to implementation details (beginning of Sec. 5) for the definition of ‘contiguous’ and ‘modulated’. The right shows the comparison on primitive growth between 3DGS [22] and 3DGS+DashGaussian on these two scenes.

isting methods, and most importantly, with the SOTA rendering quality among these methods, which we attribute to the benefit from our reformulation of 3DGS optimization.

Qualitative Results. We visualize the results of Tab. 1 in Fig. 3. Our method optimizes 3DGS within 200 seconds, while the rendering quality is still comparable to or even better than the baselines. The improvement comes from that DashGaussian effectively helps 3D Gaussians to better fit the captured observations from low to high frequency gradually with more reasonable densification.

5.2. DashGaussian Enhancing Backbones

Quantitative Results. By equipping various 3DGS backbones with DashGaussian, we demonstrate that DashGaussian generalize well to 3DGS backbones with different optimizers [32], primitive representations [47], and densification scores [5]. Results are reported in Tab. 2. The

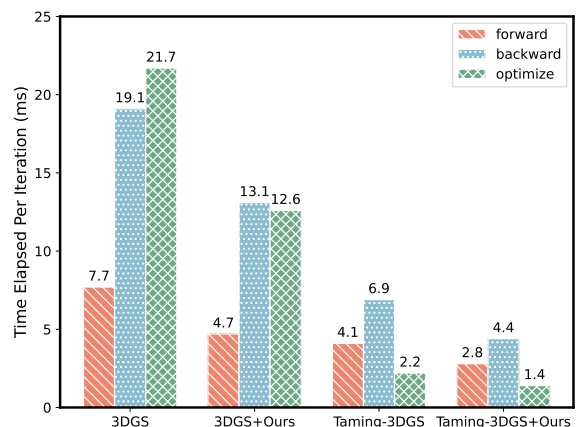


Figure 5. Profiling of the average optimization time on the Mip-NeRF 360 dataset. We can see DashGaussian effectively reduces the per-iteration elapsed time of all three major operations. It verifies that DashGaussian can effectively save the overall computational complexity of 3DGS optimization.

implementation details for each backbone are provided in the supplementary. Backbones enhanced with DashGaussian show a significant improvement in optimization speed compared with the vanilla ones, with an acceleration rate of 45.7% on average. Besides, we also notice that DashGaussian requires fewer number of Gaussian primitives in fitting scenes. Despite of the significant acceleration and reduction in primitives, the enhanced backbones preserve their rendering quality compared to the vanilla ones. The results demonstrate the effectiveness and generalization of our method, supporting DashGaussian as a plug-and-play optimization strategy that is able to be integrated into any other 3DGS baselines rather than a dedicated improvement on a specific backbone.

Visualization of Schedulers. We show the resolution scheduler and the Gaussian primitive scheduler in two dif-

ferent scenes (“bicycle” and “stump”) from the Mip-NeRF 360 dataset in Fig. 4. Specifically, on the left of Fig. 4, we compare our resolution scheduler in different scenes. Images in different scenes manifest diverse frequency information, and our method can scene-adaptively schedule the rendering resolution. On the right of Fig. 4, we compare the primitive growth between 3DGS [22] and its scheduled version (marked as “Ours”). Noticeably, our method represents scenes with fewer primitives. Please check the supplementary for more analysis on this phenomenon.

Profiling of the Optimization Time. As we pointed out in Sec. 1, the three most time-consuming operations in one optimization step of 3DGS are forward-rendering, gradient back-propagation, and primitive optimizing, respectively. We profile the average time cost of them over the whole optimization process on 3DGS [22] and Taming-3DGS [32] to see how DashGaussian affects these two backbones with different optimizer. The result is shown in Fig. 5. DashGaussian brings significant reduction on all of the three components, while the acceleration rate is almost consistent. It demonstrates that DashGaussian can substantially speed up the optimization regard less of different implementations of the 3DGS backbone.

5.3. Ablation Study

We use Taming-3DGS [32] as the backbone and individually add each module in DashGaussian to explore their effect on the rendering quality and optimization speed.

Resolution Scheduler. We keep the resolution scheduler proposed in Sec. 4.3, and remove the primitive scheduler to evaluate the resolution scheduler. The corresponding result in Tab. 3 is marked as “+Reso-Sche.”, which exhibits an allround improvement over the backbone.

Primitive Scheduler. To evaluate the primitive scheduler in Sec. 4.3, we have the primitive schedule depending on the resolution schedule while disabling the downsampling operation on training views to supervise 3DGS with the original resolution. The corresponding result in Tab. 3 is marked as “+Prim-Sche.”. Acceleration and quality improvement are similarly observed as “+Reso-Sche.”.

Full Method. We present the result of equipping the backbone with the full DashGaussian, reported as “Full” in Tab. 3. By having the two schedulers cooperating with each other, DashGaussian significantly reduces the optimization time of Taming-3DGS by 41.3%. Meanwhile, our method surpasses the rendering quality of the backbone while using fewer Gaussian primitives.

Hyper-parameters. The hyper-parameters of DashGaussian can influence the optimization time and rendering quality. We report the ablation studies on them in the supple-

Table 3. Ablation studies over the proposed scheduling schemes of DashGaussian. Experiments are performed on the Mip-NeRF 360 dataset [3] with Taming-3DGS [32] as the backbone.

Method	$N_{GS} \downarrow$	PSNR \uparrow	SSIM \uparrow	LPIPS \downarrow	Time \downarrow
Taming-3DGS	2.28M	27.61	0.821	0.210	5.51
+Reso-Sche.	2.46M	27.99	0.829	0.196	4.43
+Prim-Sche.	2.23M	27.85	0.824	0.208	4.60
Full	2.04M	27.92	0.826	0.208	3.23

Table 4. We report the primitive number N_{GS}^{bb} of the backbones, the primitive number P_{fin} predicted by our momentum-based budgeting, and the primitive number N_{GS}^{ours} of DashGaussian-scheduled backbones. Conducted on Mip-NeRF 360 dataset.

Method	N_{GS}^{bb}	P_{fin}	N_{GS}^{ours}
3DGS [22]	3.12M	3.08M	2.69M
Mip-Splatting [47]	3.97M	3.25M	3.14M
Taming-3DGS [32]	2.28M	2.39M	2.04M

mentary, especially γ and η in the momentum-based primitive budgeting method that potentially influence P_{fin} .

5.4. Primitive Growth Upperbound

We evaluate how precise our momentum-based primitive budget method can estimate the maximum primitive number of a naturally densified 3DGS. The results are reported in Tab. 4. Our method effectively estimates an approximate number of primitives to densify for different backbones, while we have N_{GS}^{ours} less than P_{fin} because there are no more primitives meeting the densification condition of the backbones. Further experiments in the supplementary demonstrate that the primitive number in the optimized DashGaussian tends to be a constant for the same scene and will not increase when P_{fin} is extremely large, which prevents DashGaussian from out of memory.

6. Conclusion

In this paper, we propose DashGaussian, a computational resource allocation method to accelerate the optimization of 3DGS. Our method innovatively formulates 3DGS optimization as a frequency component fitting process, allocates the rendering resolution and primitive number corporately, and boosts the optimization by a large margin without compromise in rendering quality. Our method can be easily plugged into various 3DGS backbones, possessing the potential as a new optimization paradigm for 3DGS. This work can also improve the feasibility of training 3DGS on large-scale, time-intensive reconstruction tasks. In the future work, we will consider integrating a more insightful analysis into the connection between the primitive number and rendering resolution as a possible direction.

References

- [1] Kara-Ali Aliev, Artem Sevastopolsky, Maria Kolos, Dmitry Ulyanov, and Victor Lempitsky. Neural point-based graphics. In *Computer Vision – ECCV 2020*, pages 696–712, Cham, 2020. Springer International Publishing. 2
- [2] Jonathan T. Barron, Ben Mildenhall, Matthew Tancik, Peter Hedman, Ricardo Martin-Brualla, and Pratul P. Srinivasan. Mip-nerf: A multiscale representation for anti-aliasing neural radiance fields. In *Proceedings of the IEEE/CVF International Conference on Computer Vision (ICCV)*, pages 5855–5864, 2021. 2
- [3] Jonathan T. Barron, Ben Mildenhall, Dor Verbin, Pratul P. Srinivasan, and Peter Hedman. Mip-nerf 360: Unbounded anti-aliased neural radiance fields. In *Proceedings of the IEEE/CVF Conference on Computer Vision and Pattern Recognition (CVPR)*, pages 5470–5479, 2022. 6, 7, 8, 12, 13
- [4] Chris Buehler, Michael Bosse, Leonard McMillan, Steven Gortler, and Michael Cohen. Unstructured lumigraph rendering. In *Proceedings of the 28th annual conference on Computer graphics and interactive techniques*, pages 425–432, 2001. 2
- [5] Samuel Rota Bulò, Lorenzo Porzi, and Peter Kotschieder. Revising densification in gaussian splatting, 2024. 2, 3, 5, 7, 11, 12, 13
- [6] Anpei Chen, Zexiang Xu, Andreas Geiger, Jingyi Yu, and Hao Su. Tensorf: Tensorial radiance fields. In *Computer Vision – ECCV 2022*, pages 333–350, Cham, 2022. Springer Nature Switzerland. 1, 2
- [7] Yujin Chen, Yinyu Nie, Benjamin Ummerhofer, Reiner Birkel, Michael Paulitsch, Matthias Müller, and Matthias Nießner. Mesh2nerf: Direct mesh supervision for neural radiance field representation and generation, 2024.
- [8] Zhiqin Chen, Thomas Funkhouser, Peter Hedman, and Andrea Tagliasacchi. Mobilenerf: Exploiting the polygon rasterization pipeline for efficient neural field rendering on mobile architectures. In *Proceedings of the IEEE/CVF Conference on Computer Vision and Pattern Recognition (CVPR)*, pages 16569–16578, 2023. 1, 2
- [9] Paul Debevec. Rendering synthetic objects into real scenes: bridging traditional and image-based graphics with global illumination and high dynamic range photography. In *ACM SIGGRAPH 2008 Classes*, New York, NY, USA, 2008. Association for Computing Machinery. 2
- [10] Xiaobin Deng, Changyu Diao, Min Li, Ruohan Yu, and Du-anqing Xu. Efficient density control for 3d gaussian splatting, 2025. 2
- [11] Daniel Duckworth, Peter Hedman, Christian Reiser, Peter Zhizhin, Jean-François Thibert, Mario Lučić, Richard Szeliski, and Jonathan T. Barron. Smerf: Streamable memory efficient radiance fields for real-time large-scene exploration. 43(4), 2024. 1
- [12] Sankeerth Durvasula, Adrian Zhao, Fan Chen, Ruofan Liang, Pawan Kumar Sanjaya, and Nandita Vijaykumar. Distwar: Fast differentiable rendering on raster-based rendering pipelines, 2023. 2, 3
- [13] Guangchi Fang and Bing Wang. Mini-splatting: Representing scenes with a constrained number of gaussians, 2024. 2, 3, 5, 6
- [14] Guofeng Feng, Siyan Chen, Rong Fu, Zimu Liao, Tao Liu, Zhilin Pei, Hengjie Li, Xingcheng Zhang, and Bo Dai. Flashgs: Efficient 3d gaussian splatting for large-scale and high-resolution rendering, 2024. 3
- [15] Guofeng Feng, Siyan Chen, Rong Fu, Zimu Liao, Yi Wang, Tao Liu, Zhilin Pei, Hengjie Li, Xingcheng Zhang, and Bo Dai. Flashgs: Efficient 3d gaussian splatting for large-scale and high-resolution rendering, 2024. 2
- [16] Andrew Fitzgibbon, Yonatan Wexler, and Andrew Zisserman. Image-based rendering using image-based priors. *International Journal of Computer Vision*, 63:141–151, 2005. 2
- [17] Sara Fridovich-Keil, Alex Yu, Matthew Tancik, Qinhong Chen, Benjamin Recht, and Angjoo Kanazawa. Plenoxels: Radiance fields without neural networks. In *Proceedings of the IEEE/CVF Conference on Computer Vision and Pattern Recognition (CVPR)*, pages 5501–5510, 2022. 1, 2
- [18] Rafael C. Gonzalez and Richard E. Woods. *Digital Image Processing (3rd Edition)*. Prentice-Hall, Inc., USA, 2006. 2
- [19] Peter Hedman, Julien Philip, True Price, Jan-Michael Frahm, George Drettakis, and Gabriel Brostow. Deep blending for free-viewpoint image-based rendering. 37(6):257:1–257:15, 2018. 2, 6, 7, 13
- [20] Xu Hu, Yuxi Wang, Lue Fan, Junsong Fan, Junran Peng, Zhen Lei, Qing Li, and Zhaoxiang Zhang. Sagd: Boundary-enhanced segment anything in 3d gaussian via gaussian decomposition, 2024. 2
- [21] Binbin Huang, Zehao Yu, Anpei Chen, Andreas Geiger, and Shenghua Gao. 2d gaussian splatting for geometrically accurate radiance fields. In *ACM SIGGRAPH 2024 Conference Papers*, New York, NY, USA, 2024. Association for Computing Machinery. 5
- [22] Bernhard Kerbl, Georgios Kopanas, Thomas Leimkühler, and George Drettakis. 3d gaussian splatting for real-time radiance field rendering. *ACM Transactions on Graphics*, 42(4), 2023. 1, 2, 3, 4, 6, 7, 8, 11, 12, 13
- [23] Shakiba Kheradmand, Daniel Rebain, Gopal Sharma, Weiwei Sun, Yang-Che Tseng, Hossam Isack, Abhishek Kar, Andrea Tagliasacchi, and Kwang Moo Yi. 3d gaussian splatting as markov chain monte carlo. In *Advances in Neural Information Processing Systems*, pages 80965–80986. Curran Associates, Inc., 2024. 2
- [24] Diederik Kingma and Jimmy Ba. Adam: A method for stochastic optimization. In *International Conference on Learning Representations (ICLR)*, San Diego, CA, USA, 2015. 5, 11, 12
- [25] Arno Knapitsch, Jaesik Park, Qian-Yi Zhou, and Vladlen Koltun. Tanks and temples: Benchmarking large-scale scene reconstruction. *ACM Transactions on Graphics*, 36(4), 2017. 6, 7, 13
- [26] Jiahe Li, Jiawei Zhang, Xiao Bai, Jin Zheng, Xin Ning, Jun Zhou, and Lin Gu. Talkinggaussian: Structure-persistent 3d talking head synthesis via gaussian splatting. In *Computer Vision – ECCV 2024*, pages 127–145, Cham, 2025. Springer Nature Switzerland. 2

- [27] Yixuan Li, Lihan Jiang, Linning Xu, Yuanbo Xiangli, Zhenzhi Wang, Dahua Lin, and Bo Dai. Matrixcity: A large-scale city dataset for city-scale neural rendering and beyond. In *Proceedings of the IEEE/CVF International Conference on Computer Vision (ICCV)*, pages 3205–3215, 2023. 1, 6, 14
- [28] Zhihao Liang, Qi Zhang, Wenbo Hu, Lei Zhu, Ying Feng, and Kui Jia. Analytic-splatting: Anti-aliased 3d gaussian splatting via analytic integration. In *Computer Vision – ECCV 2024*, pages 281–297, Cham, 2025. Springer Nature Switzerland. 2
- [29] Jiaqi Lin, Zhihao Li, Xiao Tang, Jianzhuang Liu, Shiyong Liu, Jiayue Liu, Yangdi Lu, Xiaofei Wu, Songcen Xu, Youliang Yan, and Wenming Yang. Vastgaussian: Vast 3d gaussians for large scene reconstruction. In *Proceedings of the IEEE/CVF Conference on Computer Vision and Pattern Recognition (CVPR)*, pages 5166–5175, 2024. 1, 2, 14
- [30] Lingjie Liu, Jiatao Gu, Kyaw Zaw Lin, Tat-Seng Chua, and Christian Theobalt. Neural sparse voxel fields. *NeurIPS*, 2020. 1, 2
- [31] Yang Liu, He Guan, Chuanchen Luo, Lue Fan, Junran Peng, and Zhaoxiang Zhang. Citygaussian: Real-time high-quality large-scale scene rendering with gaussians, 2024. 1, 2
- [32] Saswat Subhajyoti Mallick, Rahul Goel, Bernhard Kerbl, Francisco Vicente Carrasco, Markus Steinberger, and Fernando De La Torre. Taming 3dgs: High-quality radiance fields with limited resources, 2024. 2, 3, 5, 6, 7, 8, 11, 12, 13, 14
- [33] Ben Mildenhall, Pratul P. Srinivasan, Matthew Tancik, Jonathan T. Barron, Ravi Ramamoorthi, and Ren Ng. Nerf: representing scenes as neural radiance fields for view synthesis. *Commun. ACM*, 65(1):99–106, 2021. 1, 2
- [34] Thomas Müller, Alex Evans, Christoph Schied, and Alexander Keller. Instant neural graphics primitives with a multiresolution hash encoding. *ACM Trans. Graph.*, 41(4):102:1–102:15, 2022. 1, 2
- [35] Panagiotis Papantonakis, Georgios Kopanas, Bernhard Kerbl, Alexandre Lanvin, and George Drettakis. Reducing the memory footprint of 3d gaussian splatting. 7(1), 2024. 2, 3, 5, 6
- [36] Fabio Remondino and Sabry El-Hakim. Image-based 3d modelling: a review. *The photogrammetric record*, 21(115): 269–291, 2006. 2
- [37] Johannes L. Schonberger and Jan-Michael Frahm. Structure-from-motion revisited. In *Proceedings of the IEEE Conference on Computer Vision and Pattern Recognition (CVPR)*, 2016. 3
- [38] Steven M Seitz and Charles R Dyer. Photorealistic scene reconstruction by voxel coloring. *International journal of computer vision*, 35:151–173, 1999. 2
- [39] Yunji Seo, Young Sun Choi, Hyun Seung Son, and Youngjung Uh. Flod: Integrating flexible level of detail into 3d gaussian splatting for customizable rendering, 2024. 3
- [40] Qihong Shen, Xingyi Yang, and Xinchao Wang. Flashsplat: 2d to 3d gaussian splatting segmentation solved optimally. In *Computer Vision – ECCV 2024*, pages 456–472, Cham, 2025. Springer Nature Switzerland. 2
- [41] Yuang Shi, Simone Gasparini, Géraldine Morin, and Wei Tsang Ooi. Lapisgs: Layered progressive 3d gaussian splatting for adaptive streaming, 2024. 3
- [42] A. Tewari, J. Thies, B. Mildenhall, P. Srinivasan, E. Tretschk, W. Yifan, C. Lassner, V. Sitzmann, R. Martin-Brualla, S. Lombardi, T. Simon, C. Theobalt, M. Nießner, J. T. Barron, G. Wetzstein, M. Zollhöfer, and V. Golyanik. Advances in neural rendering. *Computer Graphics Forum*, 41(2):703–735, 2022. 2
- [43] Zhou Wang, A.C. Bovik, H.R. Sheikh, and E.P. Simoncelli. Image quality assessment: from error visibility to structural similarity. *IEEE Transactions on Image Processing*, 13(4): 600–612, 2004. 6
- [44] Zian Wang, Tianchang Shen, Merlin Nimier-David, Nicholas Sharp, Jun Gao, Alexander Keller, Sanja Fidler, Thomas Müller, and Zan Gojcic. Adaptive shells for efficient neural radiance field rendering. *ACM Trans. Graph.*, 42(6), 2023. 1, 2
- [45] Vickie Ye, Ruilong Li, Justin Kerr, Matias Turkulainen, Brent Yi, Zhuoyang Pan, Otto Seiskari, Jianbo Ye, Jeffrey Hu, Matthew Tancik, and Angjoo Kanazawa. gsplat: An open-source library for gaussian splatting, 2024. 2, 3
- [46] Hongyun Yu, Zhan Qu, Qihang Yu, Jianchuan Chen, Zhonghua Jiang, Zhiwen Chen, Shengyu Zhang, Jimin Xu, Fei Wu, Chengfei Lv, and Gang Yu. Gaussiantalker: Speaker-specific talking head synthesis via 3d gaussian splatting. page 3548–3557, New York, NY, USA, 2024. Association for Computing Machinery. 2
- [47] Zehao Yu, Anpei Chen, Binbin Huang, Torsten Sattler, and Andreas Geiger. Mip-splatting: Alias-free 3d gaussian splatting. In *Proceedings of the IEEE/CVF Conference on Computer Vision and Pattern Recognition (CVPR)*, pages 19447–19456, 2024. 2, 4, 5, 7, 8, 11, 12, 13
- [48] Zehao Yu, Torsten Sattler, and Andreas Geiger. Gaussian opacity fields: Efficient adaptive surface reconstruction in unbounded scenes. *ACM Transactions on Graphics*, 2024. 5
- [49] Gim Hee Lee Yu Chen. Dogs: Distributed-oriented gaussian splatting for large-scale 3d reconstruction via gaussian consensus. In *arXiv*, 2024. 1, 2
- [50] Richard Zhang, Phillip Isola, Alexei A Efros, Eli Shechtman, and Oliver Wang. The unreasonable effectiveness of deep features as a perceptual metric. In *CVPR*, 2018. 6
- [51] Yingji Zhong, Lanqing Hong, Zhenguo Li, and Dan Xu. Cvt-xrf: Contrastive in-voxel transformer for 3d consistent radiance fields from sparse inputs, 2024. 2

DashGaussian: Optimizing 3D Gaussian Splatting in 200 Seconds

Supplementary Material

In this supplementary material, we include explanations of the implementation details in Sec. 7, the discussion over primitive growth in Sec. 8 and furthermore extensive experiments in Sec. 9, Sec. 10 and Sec. 11.

7. Implementation Details

In this section, we elaborate on the implementation of our ground truth downsampling strategy, the modification to the learning rate, the modulation on the resolution scheduler, and how we equip DashGaussian to the each backbones.

7.1. Ground Truth Downsampling

In the LR optimization stage, DashGaussian downsamples the ground truth to supervise the LR renderings from 3D Gaussians. We choose the official anti-alias downsampling algorithm from Pytorch to downsample the ground truth images, preventing possible misguidance from aliased supervision hindering the optimization.

7.2. Learning Rate

Because the optimization scheme in DashGaussian is specifically tailored, the learning rate for 3DGS optimization should be properly scheduled to allow DashGaussian to perform the best. For all the experiments, we keep all the hyper-parameters unchanged as in the original 3DGS [22] expect the positional learning rate. We hold it constant as the initial value in the LR optimization stage, and only allow it to decay from the iteration $i = \operatorname{argmin}_i \{\lfloor r^{(i)} \rfloor = 1\}$.

7.3. Modulation for Resolution Scheduler

As we pointed out in the paper, DashGaussian allocates the iterations spent on the LR and HR optimization stage, in order to accelerate the optimization process while maintaining the rendering quality of 3DGS. To this end, we further modulate s_r to suppress the LR stage while expanding the HR stage. Specifically, we apply the natural logarithm to modulate the relative multiple for different resolutions, resulting in a fraction function

$$f(\mathbf{F}, \mathbf{F}_{r_m}, \mathbf{F}_{r_i}) = \frac{\ln(\mathcal{X}(\mathbf{F})/\mathcal{X}(\mathbf{F}_{r_i}))}{\ln(\mathcal{X}(\mathbf{F})/\mathcal{X}(\mathbf{F}_{r_m}))}, \quad (6)$$

with which we have

$$\begin{aligned} s_{r_i} &= S \cdot (1 - f(\mathbf{F}, \mathbf{F}_{r_m}, \mathbf{F}_{r_i})) \\ &= S \cdot \frac{\ln(\mathcal{X}(\mathbf{F}_{r_i})/\mathcal{X}(\mathbf{F}_{r_m}))}{\ln(\mathcal{X}(\mathbf{F})/\mathcal{X}(\mathbf{F}_{r_m}))}. \end{aligned} \quad (7)$$

Eq. (7) is the actual scheduling function we use for DashGaussian and all experiments in the paper.

7.4. Densification of DashGaussian

We explain how a densification step is performed in DashGaussian. Given an optimization step i where a densification operation is performed, we set N_{GS} as the current number of Gaussian primitives, and P_i as the desired primitive number after this densification operation. We first perform a prune operation on the primitives, resulting in N'_{GS} primitives left. Then we perform clone and split operation to those Gaussian primitives that satisfy the densification condition of the backbone while having a top $P_i - N'_{\text{GS}}$ densification score. Each primitive is cloned or split depending on its size, which follows the same routine as in 3DGS [22]. When the densification score differs, slight difference is there to adopt DashGaussian to the backbones.

7.5. Equipping DashGaussian to Backbones

When we enhance a 3DGS backbone with DashGaussian, only few modifications to the codebase are adopted, including a new learning rate schedule (see Sec. 7.2 in supplementary), the rendering resolution schedule, the primitive growth schedule, and a distinct densification operation (see Sec. 7.4). These four modifications from DashGaussian are basically common for different backbones, with slight differences in the densification operation. We introduce these differences in detail below.

3DGS [22] The original 3DGS has a densification score defined as the positional gradient of each primitive. We keep the densification score, and follow Sec. 7.4 to perform densification. The optimizer is Adam [24].

Taming-3DGS [32] At the moment of this paper is written, the codebase of Taming-3DGS has an efficient backward pass implementation with the rest same as 3DGS [22]. So the densification operation is the same as Sec. 7.4. The optimizer is Sparse Adam [32].

Revising-3DGS* [5] Because Revising-3DGS is not open-sourced, we reproduce it on top of the codebase of Taming-3DGS [32]. Notice that, Revising-3DGS demands appointing the primitive number in the final 3DGS model. To this end, we follow [5] to set P_{fin} as a constant, with our momentum-based primitive budgeting disabled. Revising-3DGS has its densification score defined as rendering error, thus the densification operation follows Sec. 7.4 the same. The optimizer is Sparse Adam [32].

Mip-Splatting [47] Mip-Splatting defines its densification scores as two different scalars, where these two scores are used together to specify the primitives to be densified. For the primitive selection in densification, we merge the

Table 5. Scene-wise quantitative results over Mip-NeRF 360 dataset [3].

Method	bicycle					garden					stump				
	$N_{GS} \downarrow$	PSNR \uparrow	SSIM \uparrow	LPIPS \downarrow	Time \downarrow	$N_{GS} \downarrow$	PSNR \uparrow	SSIM \uparrow	LPIPS \downarrow	Time \downarrow	$N_{GS} \downarrow$	PSNR \uparrow	SSIM \uparrow	LPIPS \downarrow	Time \downarrow
3DGS [22]	5.74M	25.61	0.778	0.203	24.82	5.10M	27.80	0.874	0.102	23.99	4.64M	26.91	0.784	0.207	19.87
+Ours	5.38M	25.70	0.785	0.202	14.86	3.42M	27.93	0.873	0.110	11.72	3.80M	27.32	0.797	0.201	9.64
Mip-Splatting [47]	7.82M	25.95	0.803	0.162	38.81	5.60M	27.90	0.884	0.089	32.78	5.66M	27.15	0.800	0.181	28.57
+Ours	5.42M	25.85	0.796	0.176	17.67	3.87M	28.18	0.882	0.096	14.89	4.58M	27.20	0.800	0.189	11.39
Revising-3DGS* [5]	3.20M	25.58	0.776	0.205	5.44	2.65M	27.75	0.873	0.106	6.78	3.03M	27.04	0.797	0.191	5.43
+Ours	3.20M	25.66	0.791	0.191	4.19	2.65M	27.89	0.878	0.101	4.77	3.03M	27.42	0.812	0.182	3.25
Taming-3DGS [32]	3.85M	25.58	0.766	0.226	6.95	3.07M	27.63	0.869	0.110	6.89	3.73M	26.66	0.775	0.220	5.26
+Ours	3.87M	25.81	0.782	0.210	4.38	2.46M	27.91	0.868	0.119	3.80	3.14M	27.34	0.792	0.211	2.71
Method	flowers					treehill					room				
	$N_{GS} \downarrow$	PSNR \uparrow	SSIM \uparrow	LPIPS \downarrow	Time \downarrow	$N_{GS} \downarrow$	PSNR \uparrow	SSIM \uparrow	LPIPS \downarrow	Time \downarrow	$N_{GS} \downarrow$	PSNR \uparrow	SSIM \uparrow	LPIPS \downarrow	Time \downarrow
3DGS [22]	3.36M	21.86	0.622	0.328	16.50	3.62M	22.85	0.652	0.317	17.05	1.51M	31.72	0.927	0.191	15.60
+Ours	3.22M	22.17	0.631	0.318	10.78	3.63M	23.14	0.659	0.309	12.13	1.29M	31.58	0.923	0.203	8.06
Mip-Splatting [47]	4.32M	22.06	0.656	0.266	23.80	5.01M	22.61	0.655	0.269	26.12	2.10M	31.94	0.933	0.175	21.07
+Ours	3.88M	22.13	0.648	0.282	13.76	4.60M	23.15	0.662	0.285	15.47	1.59M	32.08	0.931	0.183	9.90
Revising-3DGS* [5]	2.05M	21.56	0.625	0.286	5.46	2.17M	22.65	0.647	0.307	4.80	1.00M	30.81	0.922	0.192	4.92
+Ours	2.05M	22.05	0.648	0.279	3.88	2.17M	22.80	0.656	0.300	3.30	1.00M	31.97	0.929	0.194	2.53
Taming-3DGS [32]	2.38M	21.83	0.615	0.336	4.72	2.52M	22.92	0.649	0.330	4.81	1.11M	31.51	0.925	0.198	4.32
+Ours	2.34M	22.31	0.633	0.320	3.30	2.88M	23.33	0.658	0.315	3.60	0.90M	31.85	0.922	0.205	2.38
Method	kitchen					counter					bonsai				
	$N_{GS} \downarrow$	PSNR \uparrow	SSIM \uparrow	LPIPS \downarrow	Time \downarrow	$N_{GS} \downarrow$	PSNR \uparrow	SSIM \uparrow	LPIPS \downarrow	Time \downarrow	$N_{GS} \downarrow$	PSNR \uparrow	SSIM \uparrow	LPIPS \downarrow	Time \downarrow
3DGS [22]	1.74M	31.41	0.933	0.113	18.28	1.17M	29.12	0.915	0.178	15.08	1.24M	32.19	0.947	0.173	13.56
+Ours	1.39M	31.58	0.926	0.128	9.68	1.01M	28.90	0.910	0.188	7.31	1.06M	32.01	0.944	0.177	7.28
Mip-Splatting [47]	2.13M	31.86	0.936	0.106	23.57	1.47M	29.33	0.920	0.165	19.72	1.61M	32.41	0.951	0.157	18.01
+Ours	1.71M	31.76	0.930	0.119	12.01	1.28M	29.22	0.915	0.176	9.14	1.35M	32.32	0.946	0.164	9.21
Revising-3DGS* [5]	1.43M	31.93	0.934	0.114	7.08	0.89M	29.23	0.916	0.175	6.51	1.01M	32.26	0.947	0.166	5.11
+Ours	1.43M	31.78	0.930	0.123	3.66	0.89M	29.03	0.912	0.185	3.01	1.01M	32.03	0.945	0.169	2.58
Taming-3DGS [32]	1.68M	31.09	0.930	0.117	7.71	1.02M	29.10	0.914	0.180	4.92	1.16M	32.20	0.943	0.175	4.00
+Ours	1.21M	31.52	0.926	0.127	3.89	0.78M	29.10	0.910	0.188	2.63	0.80M	32.10	0.943	0.175	2.38

primitives selected with these two densification scores as a whole set and randomly select $P_i - N'_{GS}$ primitives from them for densification. The optimizer is Adam [24].

8. Primitive Growth of DashGaussian

8.1. Why Fewer Primitives in DashGaussian?

As we discussed in Sec. 7.4 of the supplementary, the densified primitives are selected by the vanilla densification score together with a top- k selection to control the growth of primitives. In the early LR optimization stage, the top- k selection prevents the situation where a large amount of Gaussians pass the threshold resulting in an explosion of primitive growth. In the late HR optimization stage, the optimized 3DGS is relatively stable and there are less than $P_i - N'_{GS}$ primitives passing over the densification threshold. The threshold-based densification and the top- k selection constrain each other, resulting in less densified primi-

tives in the final optimized 3DGS than P_{fin} .

8.2. Constant Primitive Number

Intuitively, P_{fin} , as the primitive number upper-bound, is likely to influence the size of the optimized 3DGS. When P_{fin} is extremely large, the primitive number N_{GS} in the optimized 3DGS is likely to explode, resulting in out-of-memory (OOM) issue. Nonetheless, thanks to the double-condition densification scheme as discussed in Sec. 8.1, we can prevent OOM when P_{fin} is arbitrarily large. Concretely, as Tab. 9 in the supplementary shows, when we remove the primitive scheduler, which is equivalent to setting P_{fin} as infinity, N_{GS} still approximates to the primitive number of the backbone. This indicates the primitive growth of DashGaussian is stable and safe. Also, one can simply remove the threshold condition and only keep the top- k selection in densification, such that N_{GS} will exactly equal to P_{fin} after the optimization.

Table 6. Scene-wise quantitative results over Deep Blending dataset [19].

Method	drjohnson					playroom				
	$N_{GS} \downarrow$	PSNR \uparrow	SSIM \uparrow	LPIPS \downarrow	Time \downarrow	$N_{GS} \downarrow$	PSNR \uparrow	SSIM \uparrow	LPIPS \downarrow	Time \downarrow
3DGS [22]	3.31M	29.09	0.901	0.244	19.47	2.32M	29.90	0.907	0.244	17.27
+Ours	2.47M	28.75	0.895	0.262	8.68	1.89M	29.84	0.906	0.249	7.64
Mip-Splatting [47]	4.13M	28.66	0.898	0.243	26.80	2.83M	29.85	0.906	0.235	20.33
+Ours	3.04M	28.80	0.899	0.255	10.73	2.06M	30.29	0.906	0.241	8.86
Revising-3DGS* [5]	2.52M	29.12	0.902	0.248	4.69	1.51M	29.96	0.909	0.248	3.43
+Ours	2.52M	29.35	0.903	0.252	2.47	1.51M	30.18	0.911	0.250	1.94
Taming-3DGS [32]	2.93M	29.24	0.905	0.241	5.38	1.72M	30.14	0.908	0.249	3.65
+Ours	2.53M	29.56	0.905	0.247	2.49	1.36M	30.49	0.908	0.249	1.91

Table 7. Scene-wise quantitative results over Tanks&Temples dataset [25].

Method	train					truck				
	$N_{GS} \downarrow$	PSNR \uparrow	SSIM \uparrow	LPIPS \downarrow	Time \downarrow	$N_{GS} \downarrow$	PSNR \uparrow	SSIM \uparrow	LPIPS \downarrow	Time \downarrow
3DGS [22]	1.08M	21.78	0.812	0.207	8.46	2.58M	25.45	0.882	0.146	12.72
+Ours	1.01M	22.01	0.806	0.223	5.91	1.85M	25.66	0.882	0.156	6.38
Mip-Splatting [47]	1.47M	21.76	0.825	0.190	11.31	3.24M	25.73	0.892	0.123	17.15
+Ours	1.18M	22.01	0.820	0.207	7.05	2.07M	25.91	0.892	0.137	8.07
Revising-3DGS* [5]	0.96M	22.10	0.823	0.211	4.18	1.68M	25.65	0.889	0.126	4.81
+Ours	0.96M	22.13	0.817	0.223	2.88	1.68M	25.56	0.888	0.129	3.43
Taming-3DGS [32]	1.07M	21.96	0.816	0.204	3.64	1.96M	25.28	0.882	0.145	4.40
+Ours	1.00M	22.22	0.817	0.208	2.75	1.39M	25.71	0.884	0.153	2.48

Table 8. Quantitative results of the ablation study over γ on Mip-NeRF 360 dataset [3], with Taming-3DGS [32] as the backbone of DashGaussian. ‘1⁻’ indicates where γ infinitely approaches 1 from below, equivalent to removing the primitive scheduler.

γ	$N_{GS} \downarrow$	PSNR \uparrow	SSIM \uparrow	LPIPS \downarrow	Time \downarrow
Taming-3DGS [32]	2.02M	27.61	0.821	0.210	5.51
1 ⁻	2.46M	27.99	0.829	0.196	4.43
0.99	2.17M	27.98	0.828	0.204	3.49
0.98 (Ours)	2.04M	27.92	0.826	0.208	3.23
0.95	1.52M	27.81	0.820	0.218	2.77
0.90	1.09M	27.67	0.809	0.237	2.41

Table 9. Quantitative results of the ablation study over a on Mip-NeRF 360 dataset [3], with Taming-3DGS [32] as the backbone of DashGaussian. $a = 1$ equals removing the resolution scheduler, which is the same as ‘+Prim-Sche.’ in Tab. 3 of the paper.

a	$N_{GS} \downarrow$	PSNR \uparrow	SSIM \uparrow	LPIPS \downarrow	Time \downarrow
Taming-3DGS [32]	2.02M	27.61	0.821	0.210	5.51
1	2.23M	27.85	0.824	0.208	4.60
2	2.05M	27.97	0.827	0.204	4.62
4 (Ours)	2.04M	27.92	0.826	0.208	3.23
6	2.00M	27.93	0.825	0.211	2.88
10	1.95M	27.91	0.824	0.213	2.79

9. Scene-wise Qualitative Results

As complementary to the Tab. 2 in the paper, we report scene-wise quantitative results on all three datasets in Tab. 5, Tab. 6 and Tab. 7, respectively.

10. Ablation on Hyper-parameters

In this section, we discuss how the hyper-parameters influence the performance of DashGaussian.

Momentum-based Primitive Budgeting. The two hyper-parameters in Eq. 5 of the paper, γ and η , directly affect P_{fin} and thus N_{GS} . Before the ablation experiment, we first analyze the inner connection between γ , η , and P_{fin} to show how we select them.

Consider when Eq. 5 of the paper is stable and P_{fin} converges to a constant, we can rewrite Eq. 5 of the paper, resulting in

$$P_{\text{fin}} = \frac{\eta}{1 - \gamma} P_{\text{add}}^{(i)}, \quad (8)$$

which reveals the inner connection between P_{fin} , γ , η and $P_{\text{add}}^{(i)}$. With the above equation, one can select γ and η based on the typical $P_{\text{add}}^{(i)}$ to expect a maximum P_{fin} . However, as introduced in Sec. 8.2 of the supplementary, N_{GS} is stable with arbitrarily large P_{fin} . So selecting γ and η is to make P_{fin} approximate to N_{GS} , which effectively functions

Table 10. The report of large-scale reconstruction results on MatrixCity dataset. Time is reported in minutes.

Method	$N_{GS} \downarrow$	PSNR \uparrow	SSIM \uparrow	LPIPS \downarrow	Time \downarrow
LargeBase	18.28M	26.51	0.858	0.186	44.22
+Ours	18.08M	26.59	0.865	0.182	25.82

the primitive scheduler to accelerate the optimization while preventing under reconstruction with an over small P_{fin} .

Since changing γ and η is essentially equivalent to changing the one parameter $\eta/(1 - \gamma)$ in Eq. (8), we only perform ablation on γ . The results are reported in Tab. 9. As analyzed in Eq. (8), a larger γ indicates a larger P_{fin} , and thus a bigger N_{GS} , higher rendering quality, and more optimization time. To notice, even when $\gamma = 1^-$ where P_{fin} is infinite (implemented as removing the primitive scheduler), the value of N_{GS} is stable and significant acceleration brought by our method is still observed.

Initial Resolution. The hyper-parameter a in Sec. 4.2 of the paper decides the initial rendering resolution at the beginning of optimization, where a larger a indicates a smaller initial rendering resolution. We report ablation on a in Tab. 8. Results show that the rendering quality is basically insensitive to a , while the optimization time significantly reduces with the increase of a .

11. Evaluation on Large-scale Reconstruction

We conduct evaluation for DashGaussian on large-scale reconstruction with the MatrixCity [27] dataset, where the backbone is Taming-3DGS [32] and the divide-and-conquer strategy follows VastGaussian [29] to split the scene into 9 blocks, denoted as LargeBase in Tab. 10. The average training time on 9 blocks is reported (rendered under 1080P). While slightly improving the reconstruction quality, DashGaussian helps the backbone to reduce the training time by 41.6% on each block. This experiment again strongly supports our claim that DashGaussian can serve as a generalized plugin to accelerate the optimization of different 3DGS backbones and can well scale up from room-scale to large-scale reconstruction.